Design Study of Double-Sided Axial-Flux Magnetically-Geared Motors for Electric Aircraft Applications

Thomas F. Tallerico[1], Justin J. Scheidler[2] and Andrew Smith[3]
NASA Glenn Research Center, Cleveland, OH, 44135, U.S.A.

Electric aircraft require advances in electric drivetrain efficiency, specific power, and reliability. In terms of mass and efficiency, mechanically-geared electric drivetrains will significantly outperform a direct drive configuration in most applications. NASA is exploring magnetically-geared drivetrains as a potential way to achieve mass and efficiency benefits over direct drive systems without the maintenance and reliability penalties of mechanical gears. In this paper, one possible topology of magnetically-geared motor, the double-sided axial-flux magnetically-geared motor (DSAMGM), is studied to quantify its achievable performance. A design tool is presented that uses a genetic algorithm to optimizes the DSAMGM's efficiency and specific torque based on electromagnetic, thermal, and mechanical calculations and simulations. To verify the tool, one example output design is refined to a preliminary design level using an independent set of high fidelity finite element simulations. The high fidelity electromagnetic, thermal, and structural results are used to verify or revise the design tool's assumptions and margins. The refined design tool is then exercised to explore the performance limits of 25 kW to 200 kW DSAMGMs. The results suggest that the topology can achieve greater than 20 Nm/kg specific torque and 97% efficiency at a 100 kW output power.

I. Introduction

Electric aircraft require high performance electric drivetrains. Mechanically-geared electric motor drivetrains will significantly outperform direct drive electric motor drivetrains in most applications; however, mechanical gearboxes have a number of wear and failure modes that necessitate the addition of oil lubrication systems and can result in increased maintenance costs and reduced reliability [1] [2]. Magnetic gears are being explored by NASA as an alternative to mechanical gearboxes in electrified aircraft applications [3] [4] [5] [6] [7]. Because magnetic gears transmit torque with magnetic fields instead of mechanical contact, they have none of the contact-related wear and failure modes that exist in traditional gears.

Magnetic gears, unlike mechanical gears, can share magnetic components with an electric motor to reduce the overall weight of a magnetically-geared drivetrain. This combination of a motor and a magnetic gear is called a magnetically-geared motor (MGM). Numerous MGM topologies have been proposed and studied for various applications [8] [9] [10] [11] [12]. Most ~~of the~~ work on ~~these~~ MGM topologies to date has been tailored toward automotive and renewable energy applications where maximizing torque density (torque per unit volume) has been the primary objective. In contrast, specific torque (torque per unit mass) is vastly more important for electric aircraft. Optimizing a magnetic gear for torque density is in many ways opposite of optimizing it for specific torque [13]. Therefore, new assessments of the various MGM topologies are required to evaluate their potential for electrified aircraft applications.

NASA presented a study of one of the possible magnetically-geared motor topologies, the outer stator magnetically-geared motor (OSMGM), in a previous paper [7]. In this paper, an alternative MGM topology, the double-sided axial-flux magnetically-geared motor (DSAMGM, Figure 1), is explored for its potential in electrified

[1] Aerospace Research Engineer, Rotating and Drive Systems Branch
[2] Aerospace Research Engineer, Rotating and Drive Systems Branch
[3] Aerospace Engineer, Thermal Systems and Transport Processes Branch

aircraft applications. This study of DSAMGM performance is carried out using a NASA-developed DSAMGM design tool. A high fidelity DSAMGM design, based on one of the design tool's output designs, is presented as verification of the design tool's performance predictions and to refine its assumptions. For comparative purposes, this design is produced at the same 100 kW power level used in [7]. Additional design studies at different power levels are presented to explore the scalability of the DSAMGM topology.

In Section II of this paper, a brief description of the working principles of the DSAMGM is given. Section III presents the developed design tool. Section IV presents a high fidelity 100 kW DSAMGM design. Section V presents results from the refined design tool to estimate the achievable performance of the DSAMGM.

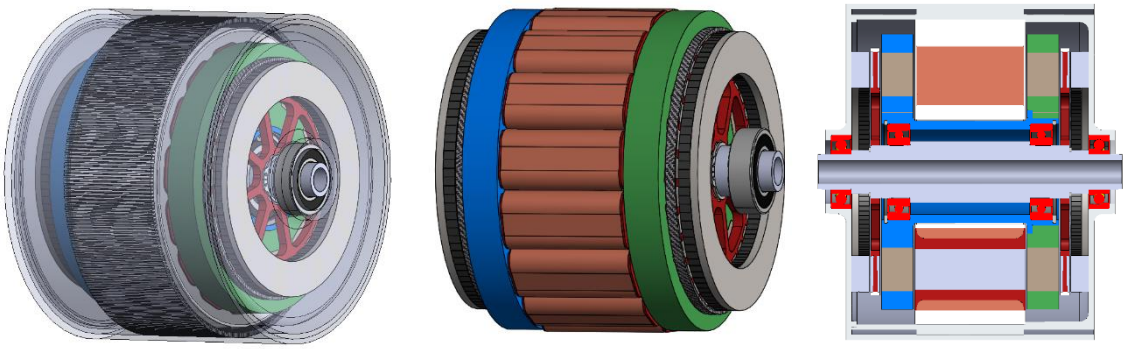

Figure 1 Example double-sided axial-flux magnetically-geared motor. Equivalent diagram with component labels in figure 2.

II. Double-Sided Axial-Flux Magnetically-Geared Motors

A DSAMGM (Figure 1) consists of two axial flux concentric magnetic gears (CMG) and a double rotor axial flux motor. The two CMGs axially sandwich the double rotor axial flux motor and use the permanent magnetic rotors of the motor as their sun gears. In this way the magnetic and mechanical mass of the motor rotors is utilized by both CMGs and the motor. Weight is thereby reduced relative to magnetically-geared motor drives that do not share components between their gears and motor. A schematic of the DSAMGM layout is given in Figure 2.

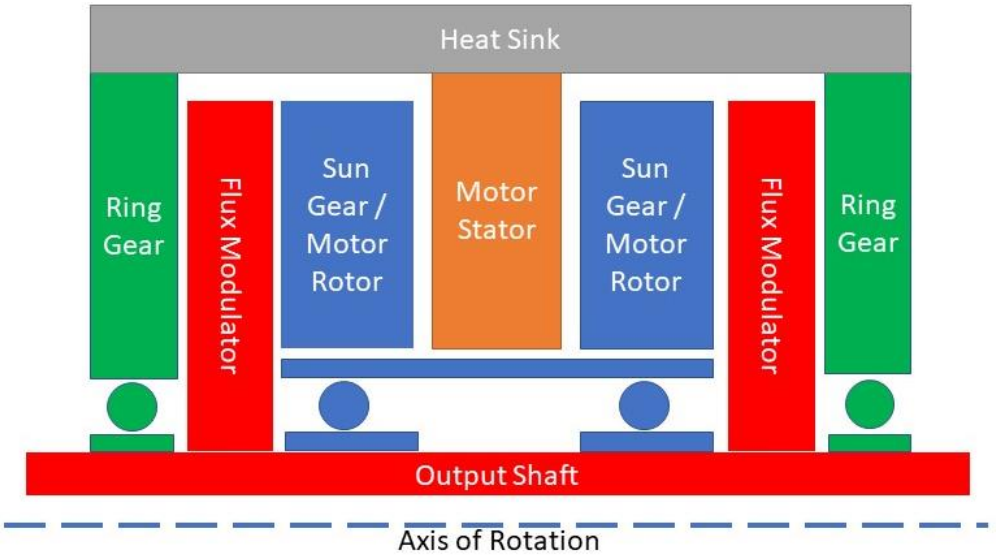

Figure 2 Mechanical schematic of a double-sided axial-flux magnetically-geared motor.

Since the operating principles of an axial flux motor are well known, the remainder of this section focusses on a brief description of CMGs. CMGs were first proposed by Attalah and Howe [14]. They consist of three rotor bodies:

a high-speed, low-pole count permanent magnet rotor body, referred to here as the sun gear; a typically stationary (or low-speed), high-pole count permanent magnet rotor body, referred to here as the ring gear; and a typically low-speed (or stationary) rotor comprised of soft magnetic pole pieces called the flux modulator. CMGs transmit torque continuously between their three rotor bodies of different pole counts using flux modulation. The flux modulator of a CMG modulates, or transforms, the spatial order of the magnetic flux produced by the permanent magnets of the sun and ring gear so that flux with matching spatial harmonic order is produced in the two air gaps of the CMG. A detailed analytical model of flux modulation in a CMG can be found in [15].

CMGs achieve the highest torque density when

$$Q = PR \pm PS, \tag{1}$$

where Q is the number of modulator pole pieces, PR is the number of ring gear pole pairs, and PS is the number of sun gear pole pairs [16]. If this equation is satisfied, a CMG will always be able to transmit torque with a gear ratio.

In a CMG, either the ring gear or the modulator can be used as the output of the gear while the other is held fixed. In this paper, in order to maximize gear ratio for a given set of sun and ring gear pole pairs, the modulator is assumed to be the output of the DSAMGM. The resulting gear ratio is defined as

$$GR = \frac{Q}{PS} = \frac{PR + PS}{PS}. \tag{2}$$

III. Double-Sided Axial-Flux Magnetically-Geared Motor Design

In order to evaluate the performance limits of a DSAMGM, a design tool was developed. Figure 3 shows a flow diagram of the developed design tool. The tool uses a genetic optimization to produce pareto fronts of DSAMGM achievable specific torque and efficiency at a given power level. Within the genetic optimization, analytical mechanical equations, 2D static electromagnetic finite element analysis (FEA), 3D static thermal FEA, and basic fluid flow equations are used to evaluate the mass, efficiency, and thermal performance of each DSAMGM design created by the optimizer. The following sections give descriptions of each of the models as they appear in the flow diagram of Figure 3.

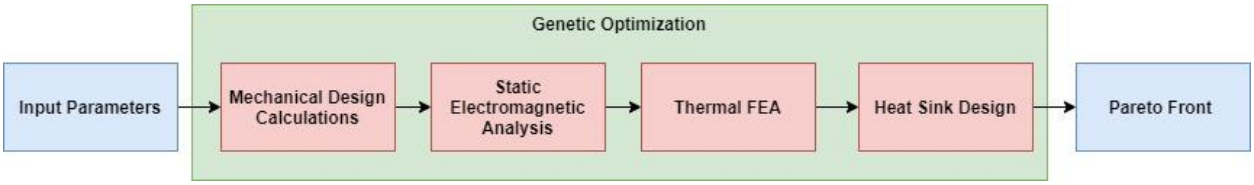

Figure 3 Flow diagram of the NASA-developed DSAMGM design tool.

A. Input Parameters, Assumptions, and Optimization Variables

To make the design tool practical, several assumptions about the MGM have to be made ahead of time. Table 1 summarizes the key assumptions and limits used to produce the results in this paper. The rationale for these assumptions is stated below. It should be noted that the intent of these assumptions is not to enable the design of the best machine possible, but to enable a realistic evaluation of this MGM topology's potential for electric aircraft applications.

Table 1 Design tool assumptions and limits.

Cooling	Liquid Cooling	**Stator Type**	Concentrated Fractional Slot
Drive	Inverter Fed	**Phases**	3
Ring Gear Magnets	Halbach Array	**Slots**	3**PS*
Sun Gear Magnet	N-S Traditional	**Slots per Pole per Phase**	0.5
Magnet Laminations	1 mm	**Wire Material**	Copper
Magnet Fill Percentage	90%	**Strand/Turn Insulation**	NEMA -MW16
Magnet Material	SmCo	**Ground Wall Insolation**	Nomex 410
Magnet Effective Br	1.0 T	**Stator Iron Material**	0.1 mm Laminated FeCo
Min. Magnet Width	2.5 mm	**Pole Piece Material**	0.1 mm Laminated FeCo
T_{avg} Winding [4]	170 °C	**Mechanical Airgap**	1 mm
Max. Winding Temperature	220 °C	**Max. Electrical Frequency**	1000 Hz

The DSAMGMs designed in this paper are assumed to be 3-phase inverter-fed machines. A limit of 1000 Hz is put on the electrical frequency of the machine to avoid optimizing machines that achieve high specific power by requiring a high performance inverter. Similarly, an iron core stator is selected to minimize the need for external inductance filters to smooth the inverter current waveform. Fractional slot concentrated windings are assumed to maximize specific power and more easily allow for the implementation of fault tolerance [17]. A half slot per pole per phase winding layout is assumed for simplicity as it works with all machine pole pair counts and enables symmetry within the electromagnetic simulations.

The DSAMGM designs are assumed to be liquid cooled via an external heat sink around the outer diameter of the machine. The details of the cooling assumptions are in Section III-E. Coolant flow losses are incorporated into the efficiency predictions. A maximum allowable winding hotspot temperature of 220 °C is assumed, corresponding to a 20 °C margin on the MW-16 winding insulation temperature class [18]. An average winding temperature of 170 °C is assumed only for resistive loss calculations in order to avoid iteratively solving winding loss predictions and thermal FEA in the design tool.

The machine is assumed to be fully sealed to avoid contamination that could lead to premature winding or bearing failure. The flux modulators and magnet rotors of the DSAMGM are assumed to only be cooled by the internal air flow that results from their rotation. Correspondingly, the magnets of the sun and ring gear are both assumed to be SmCo magnets operating at 200 °C. Every magnet is also assumed to be laminated with 1 mm thick laminations. The laminations are used to suppress magnet eddy current loss in the design. A 90% fill factor is applied to account for the non-magnetic adhesive between laminations and other assembly considerations. Considering the fill factor and operating temperature, these magnets have a remanent flux density of 1.003 T. If magnetically stronger magnets can be used in practice, for example due to the implementation of better rotor cooling strategies that enable lower magnet temperatures, significant improvements to the specific torques reported in this paper can be realized, as evidenced by [18].

The ring gears of the DSAMGM are assumed to be Halbach permanent magnet arrays. The number of magnets per pole pair is set based on having a minimum magnet width of 2.5 mm at the inner magnetic radius of the gear. The sun gears of the DSAMGM have traditional north-south magnet arrays so they can share flux with both the CMGs and the motor.

Table 2 lists the design optimization variables used in the design tool. The sun gear's tip speed, pole pair count, and electrical frequency combine to define the outer magnetic radius of the DSAMGM and the rotational speed of the sun gear. With the outer radius set, the magnetic inner radius ratio defines the inner magnetic radius of the DSAMGM. Gear ratio is determined by rounding the ratio of the sun gear's rotational speed and the output RPM optimization variable to the nearest whole number. The gear ratio and the sun gear's pole pair count then define the ring gear's pole pair count and the number of modulator pole pieces via Equations 1 and 2. Actual output speed is also calculated based on the sun gear rotational speed and the calculated gear ratio. Slot width ratio defines the ratio of winding slot

[4] Assumed average winding temperature is only for copper resistivity calculation. A value is assumed to avoid iterative thermal and electromagnetic analysis.

width to stator iron tooth width at the inner magnetic radius of the stator. Each thickness variable defines the axial thickness of the corresponding component.

Table 2 Design Tool Optimization Variables.

Optimization Variables	
Sun Gear Tip Speed (v_{tip})	Stator Electrical Frequency (f_{elec})
Sun Gear Pole Pairs (PS)	Sun Gear Magnet Thickness (t_{sun})
Modulator Thickness (t_{mod})	Ring Gear Magnet Thickness (t_{ring})
Magnetic Inner Radius Ratio (IR_{ratio})	Slot Width Ratio ($Slot_{ratio}$)
Heat Sink Fin Height (h_{fin})	Output RPM
Stator Axial Thickness (t_{stator})	Ring Gear Back Iron Thickness ($t_{ring\text{-}iron}$)
Slot Opening (tip_{gap})	

B. Mechanical Mass and Bearing Calculations

Analytical mechanical equations and basic geometric assumptions are used in the design tool to predict bearing losses and the total mechanical mass (mass of non-electromagnetic components). For simplicity and because designs produced in this paper are not tied to a specific aircraft, no propeller loads are accounted for in the mechanical design. Figure 4 shows an example structural layout of a DSAMGM. Figures 1 and 2 show the same structure as depicted in Figure 4.

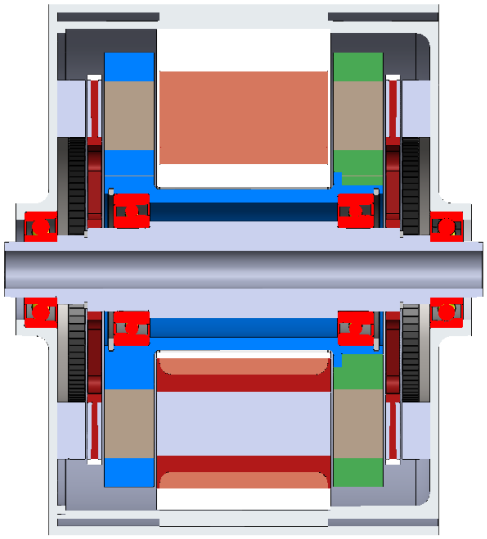

Figure 4 Example DSAMGM structural design showing assumed bearing layout.

1. Rotor Mass Estimates

Rotor masses are estimated using assumed mechanical material fill percentage and basic geometric approximations. For the sun gear, centripetal loading calculations are used to size the required carbon fiber retaining hoop for the rotor. The rest of the sun rotor's mass is predicted by assuming that it has a 75% magnetic to 25% structural composition within the radial section containing the magnets and is solid structural material outside of that region. The modulator rotor's mass is estimated assuming it has a 50% magnetic to 50% structural composition within the radial section containing the pole pieces and is solid structural material outside of that section. For both the modulator and the sun gear, the structural material was assumed to be alumina. Structural analysis of an example design is presented in Section IV-D to verify the feasibility of this approach.

The ring gear is allowed to have 100% magnetic fill in the magnetically-active region but is backed by both rotor back iron and a 3 mm thick disk of aluminum. The aluminum acts as both the ring magnet mechanical support and the end bells of the machine. The ring gear back iron is included to shield the aluminum from the sun gear's magnetic field.

2. Bearing and Shaft Design

The design tool sizes the bearings of the DSAMGM for 10,000 hours of flight at 99% reliability using the equations and recommendations in Ref. [19]. Since no propeller loads are accounted for in the tool, the dominant loads result from gyroscopic moments and accelerations caused by aircraft maneuvers. Table 3 gives the assumed values for aircraft maneuvers used in the lifing of the bearings. The same two state load case as was used in [7] is assumed.

Table 3 Assumed bearing loading cases.

Load	Max Load Case	Nominal Load Case
Pitch rate (rad/s)	2	.25
Yaw Rate (rad/s)	2	.25
X direction Acceleration (g's)	2	.5
Y direction Acceleration (g's)	2	.5
Z Direction Acceleration (g's)	3	1.25
Percent of Life	15%	85%

In addition to the maneuver loads in Table 3, rotor imbalance loads are also included in the bearing sizing. The rotors are all assumed to be balanced to an ISO G-6.3 balance grade.

Both the sun gears and modulator/output shaft are each assumed to be supported by two angular contact bearings, as is shown in Figures 2 and 4. For simplicity, in the tool, all four bearings are assumed to be the same bearing design. In reality, as is shown in Figure 4, the bearings supporting the sun gear may need to be slightly larger than the modulator/output shaft for mechanical assembly considerations. Balance of forces and moments calculations are used to calculate the loads at each bearing location using the mass and rotational inertias of the sun and modulator rotors. The design tool then evaluates all the bearings in a precision hybrid bearing database composed using [19] to determine which bearing designs are able to achieve the required life. Euler–Bernoulli beam bending equations and shaft critical speed calculations are used to determine the required radial thickness of a shaft for each bearing design that has sufficient life. A design is then selected based on minimizing the diameter of the bearings to minimize eddy current losses (i.e., to minimize the chance of the bearings being in the rotating magnetic field of the MGM). Designs for which the outer radius of the bearing is within 2 cm of the inner radius of the magnetic components are eliminated from consideration. With a bearing and shaft design selected, bearing losses are then calculated for that design at the nominal loading condition using [20]. The bearing losses are included in the efficiency prediction of the machine.

C. 2D Static Electromagnetic FEA

2D static electromagnetic FEA is used to evaluate torque carrying capacity and produce basic efficiency estimates in the design tool. The 2D geometry is a circumferential cross-section at the radial midplane of the DSAMGM's magnetic components. Integer gear ratios are used in the design tool to make the machine periodic about a single sun gear pole pair and enable the use of periodic boundary conditions in the FEA. Integer gear ratios are known to lead to high torque ripple and cogging torque in a CMG [21]. For a final design, the gear ratio would have to be updated to a non-integer value to minimize the torque ripple. Symmetry about the DSAMGM's axial midplane is also used to reduce model size. An example magnetic FEA simulation result is shown in Figure 5.

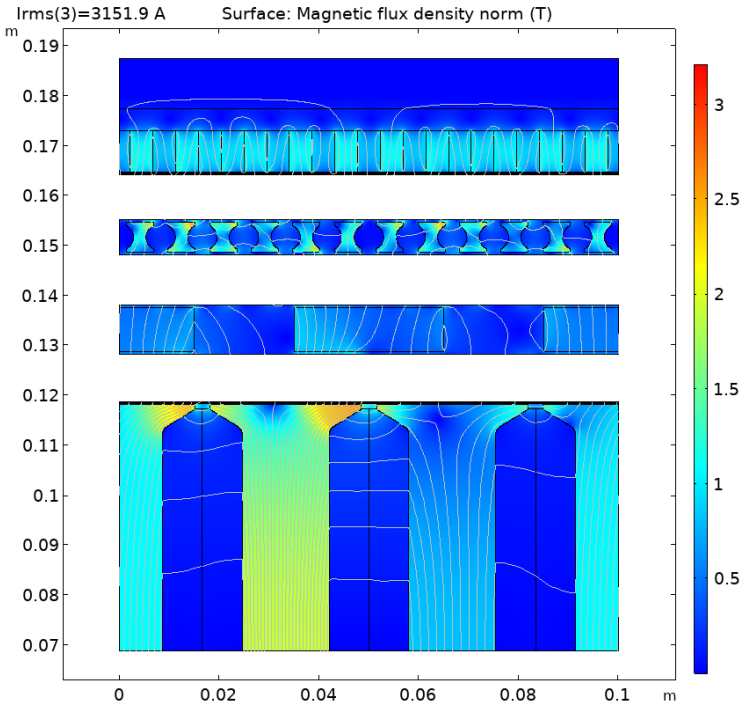

Figure 5 Example 2D FEA result from the sizing tool. Note: Rotor body boundaries are coupled together mathematically in the simulation using boundary conditions. The ~ 1 cm empty gaps between bodies is a required modeling artifact. Actual magnetic gap in the simulation is 1 mm.

To evaluate the torque characteristics of both the gear and motor portions of the DSAMGM, a parametric sweep of stator current from 0 to 22 A/mm^2 peak stator slot current density is used. Magnetic shear stresses in the ring-modulator and sun-stator airgaps are output from the FEA simulation at each evaluated stator current. Stator iron, ring gear iron, and modulator magnetic flux density data is also output at each stator current.

Motor torque at each stator current is then approximated as

$$\tau_{motor} = 2\sigma_{sun}(2\pi R)(OR - IR)R \tag{3}$$

where τ_{motor} is the motor torque, σ_{sun} is the magnetic shear stress in the sun-stator airgap, and R is the average magnetic radius. Note that this torque calculation assumes the force at the radial midplane of the DSAMGM's magnetic components is the average force along the radial direction of the gear. Motor torque and stator current values are used to create a scattered interpolant function of required current as a function of required motor torque.

Similarly, gear torque is calculated at each stator current as

$$\tau_{gear} = \left(\frac{GR}{GR - 1}\right) 2\sigma_{ring}(2\pi R)(OR - IR)R \tag{4}$$

where τ_{gear} is the gear torque and σ_{ring} is the magnetic shear stress in the ring-modulator airgap. Gear torque and stator current values are used to create a scattered interpolant function for gear torque as a function of stator current. This function is essentially a constant function since there is a very large effective airgap between the motor stator and the ring gear, but there is a minor increasing trend for gear torque with increased stator current.

The magnetic field data for the modulator pole pieces, ring gear iron, and the stator teeth are also turned into scattered interpolant functions of the stator current. The motor torque scattered interpolant function is used to define the required stator current based on the target power of that design tool iteration. The required stator current is then plugged into the other scattered interpolant functions to predict gear torque, stator tooth peak magnetic flux density, ring gear iron peak magnetic flux density, and modulator peak magnetic flux density for the design at the desired

operating point. The magnetic field data is used to estimate the DSAMGM's iron losses and ring gear magnet losses, as described in Appendix A.

A margin is held on required gear torque in the design tool to account for 3D magnetic flux leakage effects, which are common in magnetic gears, and over torque margin. In the initial evaluations of the tool, this margin was 20%; however, based on the results of the 3D electromagnetic FEA of the example design (Section IV-B), the value was later increased to 40%. If the design tool's 2D analysis predicts that a given design can't achieve the required torque plus this margin, that design is discarded in the optimization.

D. Thermal FEA

Thermal FEA is carried out on a 3D wedge of each DSAMGM geometry. Symmetry at the axial midplane as well as the periodicity of the geometry in the circumferential direction are used to reduce model size. The geometry used in the simulation is depicted in Figure 6. An example FEA result for the same geometry is shown in Figure 7.

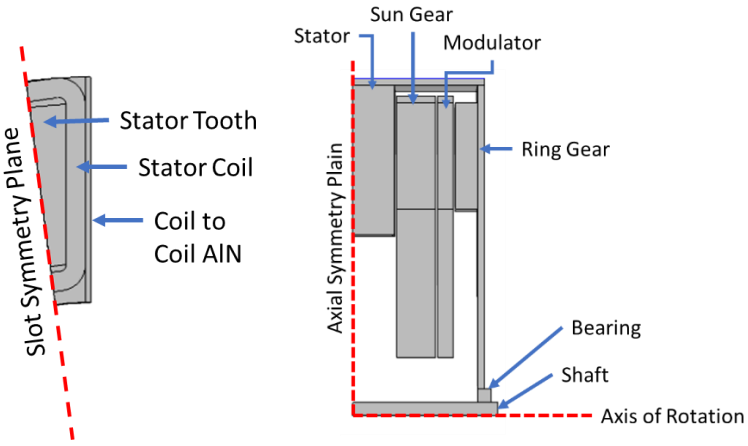

Figure 6 Geometry evaluated in the design tool's thermal FEA. (left) the stator geometry. (right) the full MGM geometry used. AlN is aluminum nitride.

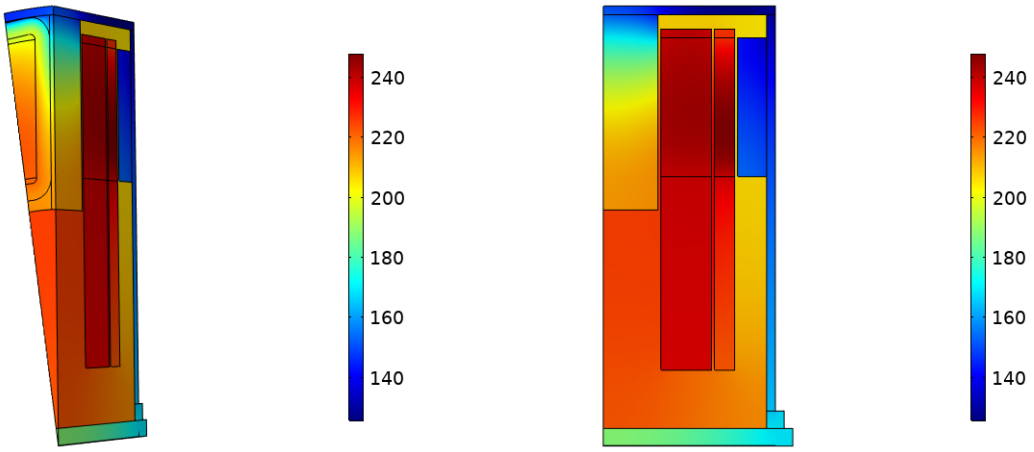

Figure 7 Example result from the design tool's thermal FEA.

To capture the heat transfer between the rotors and the stationary components of the MGM, the internal air of the machine is included in the geometry, as shown in Figure 7. This internal air volume is modeled as a high conductivity solid with thermal contact resistances applied at its boundaries with the DSAMGM's solid body components. These contact resistances are used to approximate the convective heat transfer between the solid bodies and the air. In this modeling approach, the air volume essentially acts as a control volume of uniform temperature that the rotors and stator transfer heat to based on convection coefficient correlations. The convection coefficients, which are applied as

thermal contact resistances on the rotor and stator faces, are approximated using the Nusselt number correlations for enclosed rotating disks found in [22].

For each thermal simulation, a parametric sweep of effective external convection coefficient is run. Peak winding temperature versus external convection coefficient is taken from the model and used to evaluate the performance of heat sink designs, as described in the following section; an example result is shown in Figure 8. The predicted temperature of the magnets and the bearings are not used in this iteration of the design tool.

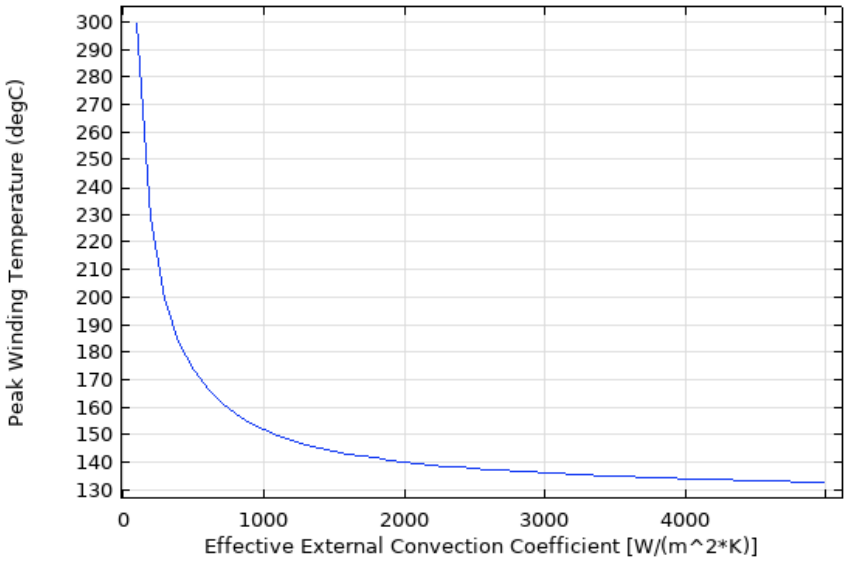

Figure 8 Example thermal FEA result: peak winding temperature versus effective external convection coefficient.

Initial results of this model pointed to the stator temperature being thermally limiting for the achievable specific power and torque of the machine. This was primarily due to the radial thermal resistance of the end windings of the machine limiting conduction of heat from the windings to the external heatsink. To combat this, an aluminum nitride finned skeleton was implemented into the design that filled the tip gap space between coils (see Figure 6) and improved the radial thermal conductivity of the stator (see Figure 7). The thickness of these fins was controlled by the tip_{gap} optimization variable. In theory, these fins could be used as phase-to-phase insulation and structural support for the winding, but neither of those considerations were accounted for. The polyimide winding insulation was still sized as if the aluminum nitride wasn't there. Alternative methods could have been used for improving the thermal conductivity of the winding, but this method had the best synergy with what was assumed in the OSMGM design paper [7], where the end winding supports were assumed to be made of aluminum nitride.

E. Liquid Cooling Jacket Design

For each geometry analyzed by the design tool, an axial flow liquid cooling jacket is designed to optimize thermal and efficiency performance of the machine. A heat sink design algorithm is used to evaluate the cooling performance and fluid flow losses of multiple possible designs based on different combinations of coolant temperature rise, heat sink fin count, and heat sink fluid channel width. The algorithm's design variables and assumptions are listed in Table 4.

Table 4 Assumptions used in the heat sink design algorithm.

Heat Sink Type	**Axial Flow**	Coolant Inlet Temperature	**80 ˚C**
Fin Height	Input Variable	**Min Coolant Temperature Rise**	0.001 ˚C
Min Fin Width	1 mm	**Max Coolant Temperature Rise**	3 ˚C
Max Fin Width	10 mm	**Coolant Thermal Conductivity**	0.1 W/(mK)
Min Fluid Channel Width	1 mm	**Coolant Viscosity**	30 cSt
Min Number of Channels	10	**Coolant Density**	900 kg/m^3
Inner and Outer Wall Thickness	3 mm	**Heat Sink Material**	Aluminum

The algorithm assumes that the flow is distributed upstream of the DSAMGM in the propulsion system's thermal management system (TMS) and arrives at the DSAMGM distributed uniformly around its outer diameter. Manifold calculations to distribute the flow are therefore neglected. Full system (DSAMGM, motor controller, and TMS) analysis is needed to evaluate whether this assumed TMS flow path is valid for the optimum propulsion system performance.

An oil with conservative thermal performance is used as the cooling fluid in the design tool, because it is assumed that other aircraft systems may require oil or that some of the DSAMGMs might be connected to a mechanical gearbox as the final stage in the drivetrain. Again, detailed system analysis would be needed to determine if this assumption makes sense or if a higher quality thermal fluid could be used to cool the machine without significant system level penalties. Air cooling is also possible with an MGM but was not explored in this paper.

The calculations used to evaluate the heat transfer coefficient on the walls of the cooling jacket and the coolant flow losses are detailed in Appendix B.

IV. High Fidelity 100 kW Design

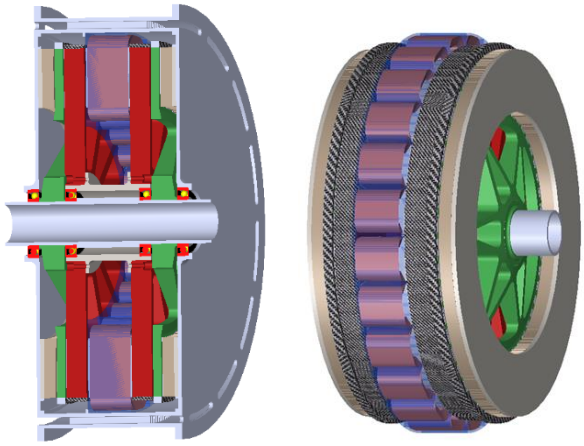

Figure 9 High fidelity DSAMGM design.

From an initial design tool run, a design was selected for higher fidelity structural, thermal, and electromagnetic analysis. The results of the higher fidelity analysis were used to evaluate the accuracy of the design tool's performance predictions and adjust some of its assumptions. Figure 9 depicts the geometry of the selected design. Table 5 gives the variables that define the design. Table 6 presents the design tool-predicted losses of the design. The following sections present the results of the high fidelity analysis of the design and compare them to the design tool's results.

Table 5 Selected design tool-generated DSAMGM design for high fidelity analysis.

High level Variables			
Power (kW)	100	Specific Power (kW/kg)	2.4
Efficiency	97%	Specific Torque (Nm/kg)	19.75
v_{tip} (m/s)	102	PS	8
f_{elec}	928	Sun RPM	6962
GR	6	Mod RPM	1160
Geometry Variables			
t_{sun} (mm)	17.4	IR_{Ratio}	66.0%
t_{mod} (mm)	7.3	t_{stator} (mm)	37.6
t_{ring} (mm)	9.8	$Slot_{ratio}$	74.8%
$t_{ring\text{-}iron}$ (mm)	3.4	tip_{gap} (mm)	3.3
Winding Info			
Wire Gage	32	Turns per Slot	71
Slot Fill	39.7	Transvers Thermal Cond. (W/mK)	3.4
Heat Sink Design			
h_{fin}	6	Volumetric Flow (m^3/s)	7.00E-03
# of Channels	282	Wall Convection Coe. (W/m^2K)	157
Channel Width	2.4	Effective convection Coe. (W/m^2K)	780

Table 6 Design tool predicted losses and efficiency of the high fidelity design.

Loss and Efficiency		
	Per Rotor	**Total**
Sun Magnet Loss (W)	50	100
Modulator Loss (W)	91	182
Ring Magnet Loss (W)	36	72
Ring Iron Loss (W)	67	134
Stator Iron Loss (W)	1413	
I^2R (W)	1119	
Proximity (W)	0.53	
Bearing (W)	20.35	
Sun Stator Windage (W)	24	48
Sun Mod Windage (W)	14.5	29
Mod Ring Windage (W)	0.175	0.35
Pumping Loss (W)	0.327	
Loss (W)	3046.6	
Efficiency	97.04%	

A. Pseudo-Transient 2D Electromagnetic Analysis

A pseudo-transient, time stepping analysis of the design was completed to raise the fidelity of the magnetic loss predictions and compare them to the loss values predicted by the design tool. 121 static simulations of the 2D electromagnetic geometry of the design at the radial midplane were used to approximate the time-dependent magnetic field in the magnetic components. The 121 snapshots of the machine's motion were evenly spaced over one electrical period of the sun gear with sun gear position, modulator position, and stator current all set to maintain full load angle in the gear and motor. Magnetic field data was extracted from each simulation using a 0.25 mm grid and used to compose an estimate of the time-varying magnetic field in each magnetic component over one sun gear electrical period at the machine's nominal rotational speed. Magnetic losses in the various components were then calculated as described in Appendix C. The resulting loss values from the analysis are listed in Table 7.

Table 7 Magnetic losses of the high fidelity design predicted by a 2D pseudo-transient FEA.

Loss Component	Per Rotor	Total
Sun Magnet Loss (W)	60	120
Modulator Loss (W)	114	228
Ring Magnet Loss (W)	38	77
Ring Iron Loss (W)	215	430
Stator Iron Loss (W)	915	
Proximity (W)	3.75	

For the DSAMGM's magnetic gear components, the pseudo transient analysis predicts higher losses than the design tool (compare Tables 6 and 7). This is expected because the pseudo-transient analysis is able to capture losses caused by temporal magnetic flux with higher harmonic order, whereas the design tool's static analysis only accounts for the fundamental frequencies in its loss predictions. Ring iron loss is the only magnetic gear loss component for which significant error exists between the design tool and pseudo transient analysis results. No clear reason for this error could be determined, so whether the error was in the static or the pseudo-transient analysis is unknown. Corrections in the design tool were therefore not applied for this error, but it should be noted that this is a possible source of inaccuracy in the design tool results in Section V.

The stator iron loss is the other noted point of significant error comparing Table 7 to Table 6. This error is attributed to an over prediction of the stator iron mass in the design tool, which was corrected. With the correction applied, the design tool predicts 925.6 W of stator iron loss. Total magnetic losses, with the correction accounted for, differ by 360 W between the design tool and pseudo-time stepping analysis. About 300 W of this difference is in the ring gear iron loss.

B. 3D Static Electromagnetic Analysis

As mentioned above, 3D magnetic flux leakage is significant in magnetic gears due to the large effective air gaps and interactions between the sun and ring gear magnetic arrays. No known correlation or extensive data exists in the open literature for the relationship between 2D and 3D FEA torque predictions for axial magnetic gears. In the initial design tool run used to produce the high fidelity design, only a 20% margin was held on 2D FEA-predicted gear torque to account for both 3D leakage and over torque margin. To assess whether this margin was sufficient, a 3D electromagnetic analysis of the design was completed. The geometry of the model and flux result plots are shown in Figure 10. As was done in the 2D model, the 3D model takes advantage of the axial symmetry and circumferential periodicity. A mesh refinement study with a linear iron model was run to select the mesh size for solving a version that utilized a nonlinear iron model. Both the results of the linear iron and the nonlinear iron models are summarized in Table 8. All cases were run with 1000 A RMS stator current and full load angle in the motor and gear halves. The permanent magnets were modeled in the same manner as the 2D electromagnetic models – a linear magnetic response with remanent flux density of 1.003 T.

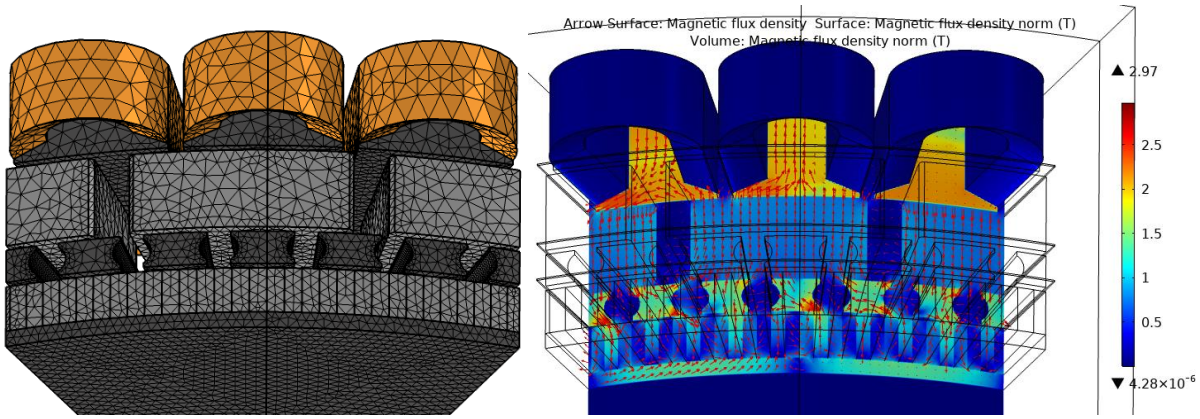

Figure 10 3D electromagnetic model geometry (left) and example magnetic flux result from the same perspective.

Table 8 3D electromagnetic model mesh refinement results and final (nonlinear iron) results.

Iron Model	# DOFs	Motor Torque (Nm)	Gear Torque (Nm)	Gear ratio
Linear Iron	1,052,441	130.44	832.26	6.07
	2,261,557	131.49	829.57	6.04
	3,050,807	131.55	828.95	6.03
	6,196,129	131.56	828.72	6.03
Nonlinear Iron	3,304,027	133.67	824.96	6.07

The mesh refinement studies show little variation in predicted torque with improved mesh in Table 8. The final run of the model with the nonlinear iron took approximately 34 hours on a high performance engineering desktop. The resulting torque prediction for the motor is below the required value by 4 Nm at 1000 A RMS. Assuming a linear relationship between motor torque and current, this indicates that 1030 A is required to produce the desired torque. The design tool's prediction is 950 A. For this case, the design tool's prediction of stator conduction (I^2R) loss is therefore low by about 17%. Hence, the design tool was revised by adding a 10% margin to its motor torque prediction. This revision was implemented for the design tool results in Section V.

The gear torque in Table 8 for the nonlinear iron case is only about 1 Nm higher than the required torque. So, although the original 20% margin on gear torque in the design tool was sufficient to account for 3D leakage, there is no over torque margin. To ensure adequate conservativism, the design tool's margin on gear torque was revised to 40%. This revision was also implemented for the results in Section V.

It should be noted that for both the motor torque and gear torque, margins were applied based on only analysis of this one example design. Whether the margins are appropriate for other design cases is unknown; however, the computational cost of 3D, nonlinear magnetic FEA analysis is too significant to include in the design tool for this initial assessment of the technology. As long as the uncertainty in 3D flux leakage over the design space is noted when viewing the results of Section V, the results should be reasonable for understanding the potential of the DSAMGM for aircraft applications. A potential compromise for future versions of the design tool could be to include the 3D simulation with linear iron model, which solved in about 10 minutes. In the case considered here, the iron nonlinearity only caused a 0.5% and 1.6% change in gear and motor torque.

C. Thermal Analysis

The thermal FEA component of the design tool (section III-D) relies on Howey [22] to estimate convection heat transfer interfaces between the DSAMGM components and the internal air volume of the machine. To check the accuracy of the internal component temperatures predicted using this method, a high fidelity CFD and heat transfer model of the example DSAMGM design was completed. To reduce computational costs relative to a fully conjugate model, a decoupled approach was used where the CFD heat transfer model of the internal air was solved first and then thermal heat flux boundary conditions calculated from that CFD model were applied in a solid body thermal model to obtain a higher fidelity prediction of component temperatures. Figure 11 shows a velocity vector plot for the CFD model of the internal air.

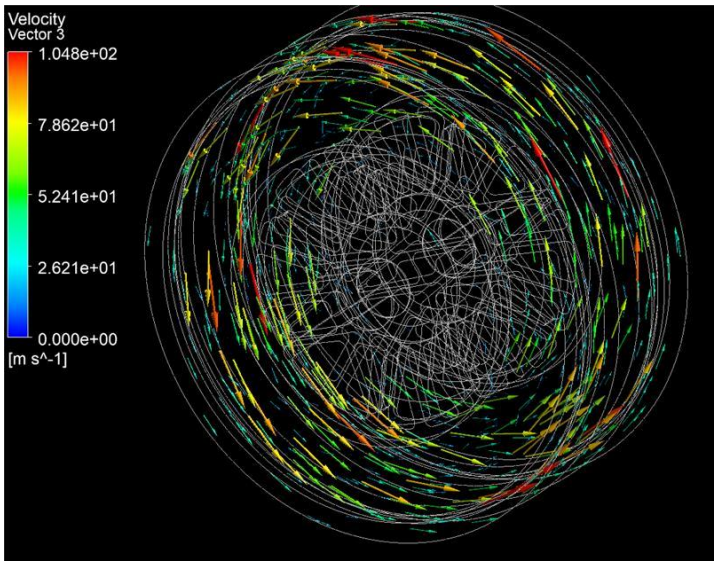

Figure 11 Velocity vector cloud from the internal CFD model.

The focus of the internal air CFD model was on the distribution of internal air temperatures and convection heat transfer coefficients on the rotor surfaces. To obtain an accurate characterization, a moving-boundary RANS model was constructed using a widely available commercial CFD code. The complex rotor face and spoke geometries of the DSAMGM are not conducive to frozen rotor study, so a fully-transient moving mesh solution was necessary. Energy source boundary conditions were applied at the appropriate locations for the rotor heat sources. Stator heat was neglected in the internal air characterization assuming the stator has a temperature similar to that of the internal air and most of its heat is transferred conductively to the heat sink. The deforming mesh solution was marched forward in time while monitoring time-averaged temperatures within the air gaps. Air gap temperatures stabilized within about 2.09 seconds of simulation time, or about 1130 accumulated time steps. Plots of the resulting fluid flow and internal air temperature distribution at a section plane through the DSAMGM are depicted in Figure 12.

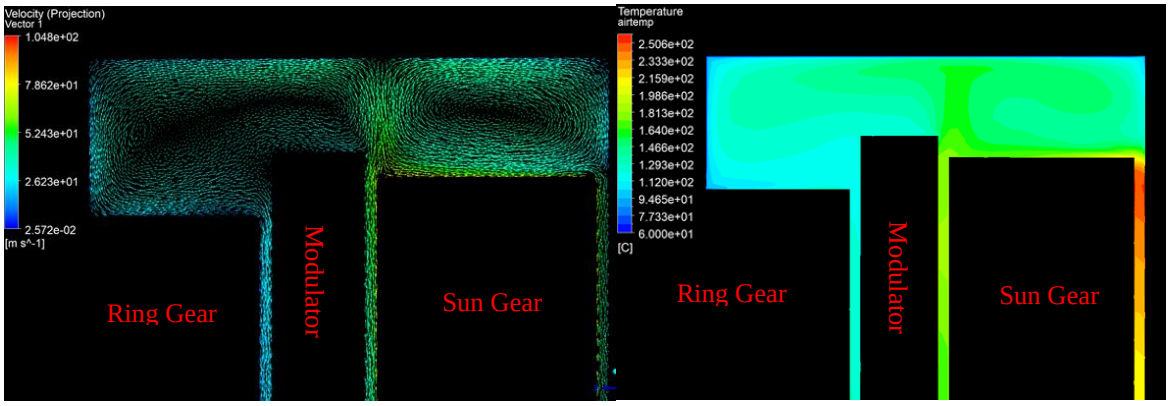

Figure 12 Cross sections of the CFD model of the DSAMGM's internal air: velocity (left) and temperature (right) distributions.

In the velocity plot of Figure 12, the internal air is shown to be pumped radially outward through the two air gaps next to the high speed sun gear (7,000 RPM) and returns radially through the ring gear (0 RPM) to modulator (1,600 RPM) air gap. The flow loop is completed axially through the holes in the modulator and sun gear rotor hubs. Also in Figure 12, a large recirculating region outboard of the sun gear and modulator can be seen and correlated with the temperature distribution in the same region. A peak air temperature of 250 °C is located at the edge of this circulating region in the sun-to-stator air gap.

From the CFD solution, contours of convective heat transfer coefficients and near-wall air temperatures were applied as boundary conditions in a fully-detailed, solids-only model of the DSAMGM. An example of the exported convection coefficients is shown in Figure 13 on a section of the DSAMGM sun gears.

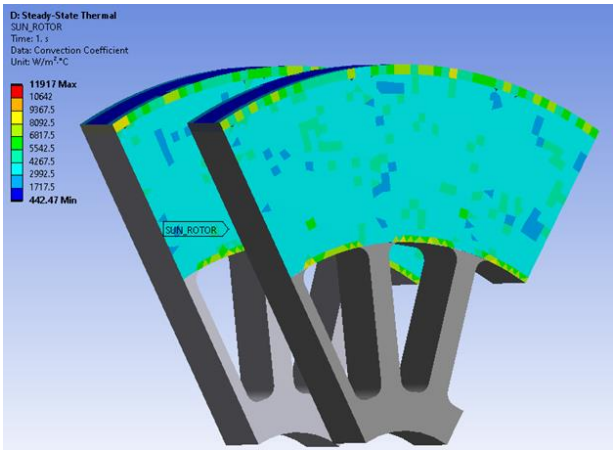

Figure 13 Imported contours of heat transfer coefficient from the time-averaged CFD solution, as applied to the active surfaces of the sun gears.

Volumetric heat loads were applied to each solid body component (stator, sun magnets, modulator magnets, and ring gear) in the solid body model corresponding to the heat loads from Table 7 and resistive winding losses predicted from the 3D electromagnetic FEA. The resulting steady-state thermal solution for the sun gear and stator are shown in Figure 14. Peak temperatures from all magnetic components are summarized and compared to the design tool FEA result in Table 9.

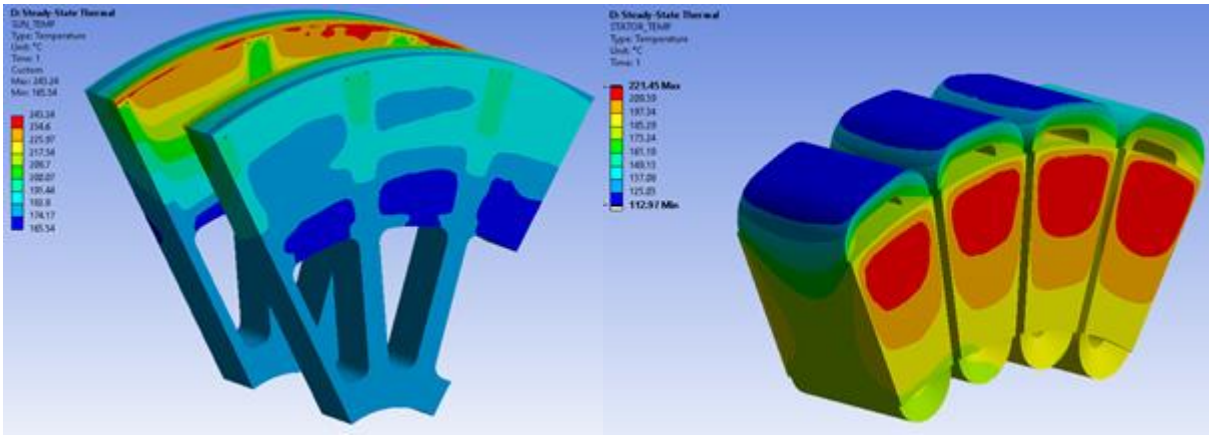

Figure 14 Contours of steady-state temperature for the sun gear (left) and stator windings and iron (right).

Table 9 Peak temperature comparison between high fidelity conjugate model and design tool thermal models of the DSAMGM.

Component ID	Peak Temp., Thermal FEA Design Tool	Peak Temp., Conjugate Heat Transfer Model
Stator Windings	~220 [°C]	211 [°C]
Sun Magnets	~240 [°C]	243 [°C]
Modulator Pole Pieces	~245 [°C]	161 [°C]
Ring Magnets	~150 [°C]	155 [°C]

The only component with significant temperature difference between the high fidelity thermal model and the design tool's thermal model is the modulator pole pieces. They are predicted to actually have significantly lower temperature than the design tool's prediction. This temperature difference between the two models is the result of the higher flow velocity in the modulator-ring gear air gap in the CFD model resulting from the recirculation of the sun gears radially pumped flow, as shown in Figure 12. The effect of the sun gear on the flow in this air gap is neglected in the design tool's thermal model. Correspondingly better coupling between ring and modulator temperature is seen in the high fidelity model than in the design tool thermal model. This error is not a point of concern as it is a lower temperature and the focus of the design tool's thermal model is on motor winding temperature for which there is good agreement between the two models. No corrections to the design tool's thermal model were applied as a result of this analysis.

D. Structural Analysis

The two components of primary concern structurally within the DSAMGM are the sun gear and modulator of the machine. Both components are magnetic rotors that are nested axially between two other magnetic components. They experience axial, tangential, and centripetal loading while having minimal space for structure. Additionally, the structures for both rotors have to be made of non-magnetic and non-electrically conductive materials to minimize eddy current loss caused by the 3D leakage effects and time-varying field passing axially through the components.

Structural design and analysis of these two rotors was carried out for the high fidelity DSAMGM design to show the mechanical feasibility of the DSAMGM. CAD of the full machine (Figure 9) was also created for a mass comparison to the design tool prediction. The components were only modeled to the preliminary design level, meaning details like bolts and shaft splines were neglected for this feasibility assessment. The structural design of both the sun gear and the modulator are shown in Figures 15 and 16, respectively.

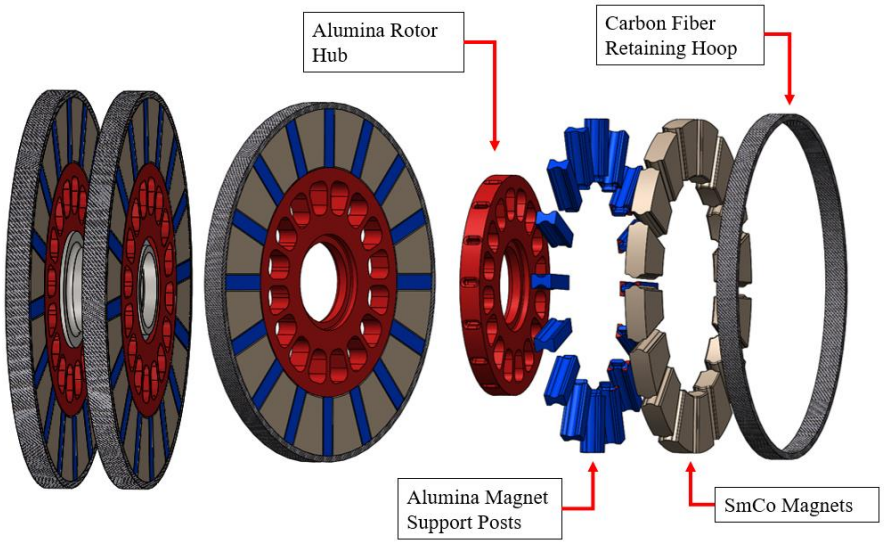

Figure 15 Sun gear rotor structural design.

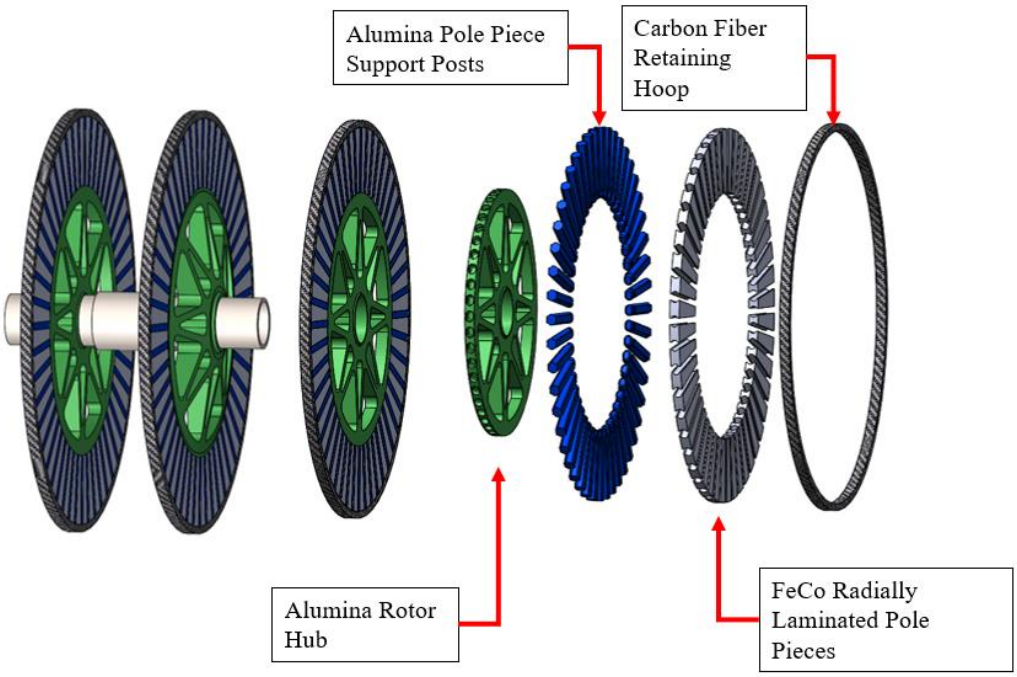

Figure 16 Modulator Rotor Structural Design.

For both modulator and sun gear rotors, the bulk of the structure was modeled as alumina for this rotor feasibility assessment. Generally ceramic materials are a good choice for the structures of magnetic gears, because they have high thermal conductivity, high stiffness, decent mechanical strength, and low electrical conductivity. There are however significant concerns about the fracture toughness of the ceramics and the cost of producing the ceramic structures. Alternative materials could be fiberglass and carbon fiber composite. Fiberglass composites will perform worse thermally and potentially have stiffness issues relative to ceramic. Carbon fiber composites will also have lower stiffness and potentially add some eddy current loss to the machine, although it is difficult to quantify how much. If the previously discussed material options are not feasible, metals could be used in the rotor hubs, but 3D transient electromagnetic modeling would be needed to quantify the loss penalty in that case.

The geometry used for the rotors in the structural FEA is pictured in Figure 17. In both cases, symmetry was used to model only an arc segment corresponding to one sun gear pole pair of the machine. Additional symmetry could have been used on the sun gear at the axial midplane of the assembly. Symmetry at the axial midplane of the modulator could not be used since torque is only output from the DSAMGM at one end of the modulator's shaft.

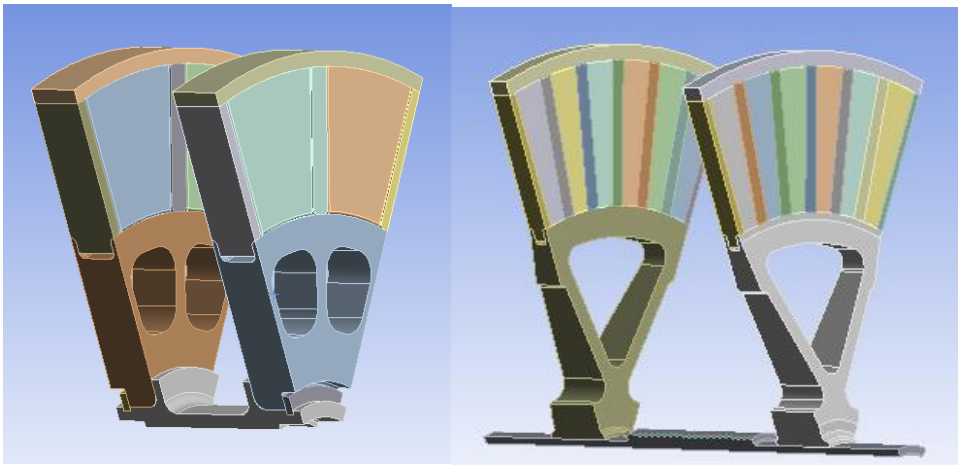

Figure 17 Sun gear and modulator geometry used in the structural FEA.

Worst case axial loads on the magnetic components of the two rotors were taken from the pseudo-transient FEA of Section IV-A. Thermal expansion of the rotor components up to 200 °C was included. A tangential force corresponding to the DSAMGM output torque was applied to the modulator pole pieces. No tangential force was applied to the sun gear since no net magnet torque is produced by the rotor. The resulting stress distribution for both rotors is shown in Figure 18 below.

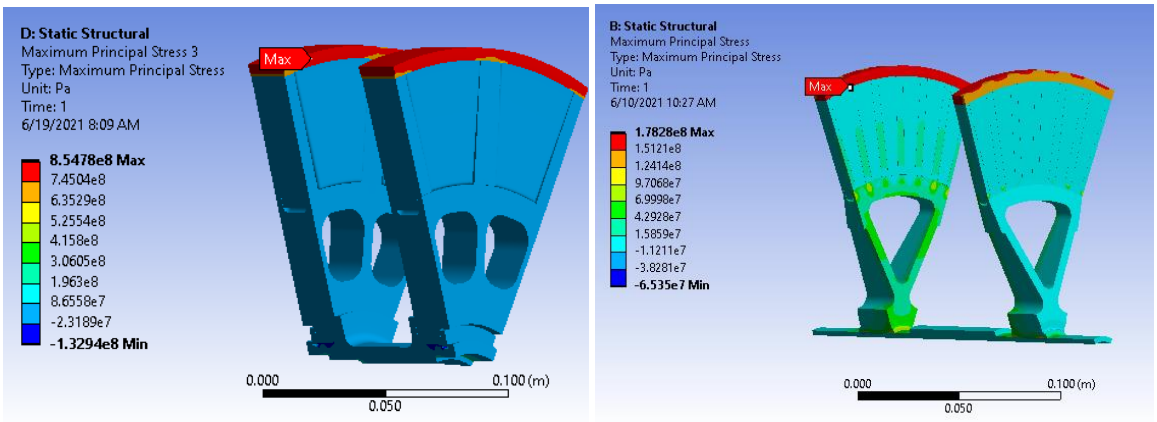

Figure 18 Maximum Principle Stress Result for Both Sun Gear and the Modulator.

In Figure 18, both rotors are shown to have their peak stresses in the carbon retaining hoop and be relatively lightly loaded in the magnetic and alumina components. Tables 10 and 11 summarize the peak stresses in the main rotor components and the corresponding equivalent safety factors relative to the material strengths.

Table 10 Sun gear component stresses and equivalent safety factors.

Component	Max Stress	Equivalent Safety Factor
Rotor Body	100 MPa	2.62
Rotor Magnet Support Posts	155 MPa	1.69
Magnets	17.8 MPa	2.08
Retaining Hoop	854 MPa	1.94

Table 11 Modulator component stresses and equivalent safety factors

Component	Max Stress	Equivalent Safety Factor
Rotor Body	168 MPa	1.56
Pole Piece Support Posts	117 MPa	1.62
Pole Pieces	22 MPa	~
Retaining Hoop	178 MPa	>10

In Tables 10 and 11, at least a 1.5 equivalent safety factor is shown to be achievable for all components, demonstrating at least the feasibility of the machine's structural design. According to the CAD model, the total mass of the machine after preliminary structural design is 39.71 kg. This is 6% larger than the design tool's prediction of 37.36 kg (with stator iron mass corrected). The error could likely be eliminated with more mass optimization of the DSAMGM structure. No correction on masses was applied in the design tool as a result of this analysis.

V. Design Tool Results

With the design tool's margins updated and corrections applied based on the high fidelity design analysis in section IV, the tool was exercised for power levels of 25, 50, 100, 150, and 200 kW. The initial bounds of the optimization variables used in the design studies are summarized in Table 12. These bounds were tightened as more understanding

of the design space was gained with each run of the tool. Trends of efficiency versus specific torque and radius versus specific torque are shown in Figures 19 and 20 for the design study results.

Table 12 Optimization variables for the revised design tool.

Sun Gear Tip Speed (v_{tip})	50-200 m/s	**Stator Electrical Frequency (f_{elec})**	750-1000
Sun Gear Pole Pairs (PS)	4-10	**Sun Gear Magnet Thickness (t_{sun})**	5-20 mm
Modulator Thickness (t_{mod})	4-10 mm	**Ring Gear Thickness (t_{ring})**	4-12 mm
Magnetic Inner Radius Ratio (IR_{ratio})	0.60-0.70	**Slot Width Ratio ($Slot_{ratio}$)**	0.30-0.80
Heat Sink Fin Height (h_{fin})	4-10 mm	**Output RPM**	1000-4000
Stator Axial Thickness (t_{stator})	20-100 mm	**Ring Gear Back Iron Thickness ($t_{ring\text{-}iron}$)**	0-10 mm
Slot Opening (tip_{gap})	1-5 mm		

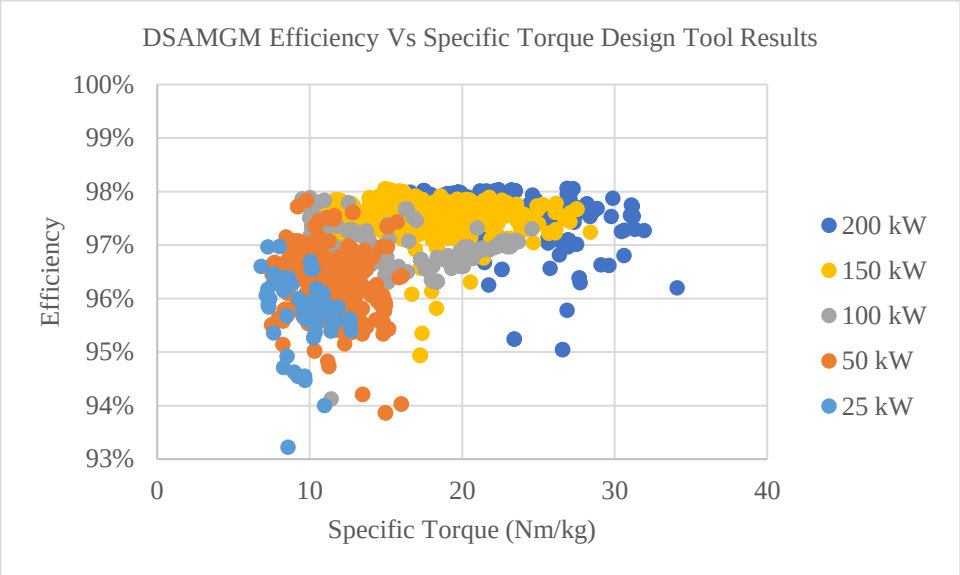

Figure 19 Efficiency versus specific torque results from the revised DSAMGM design tool.

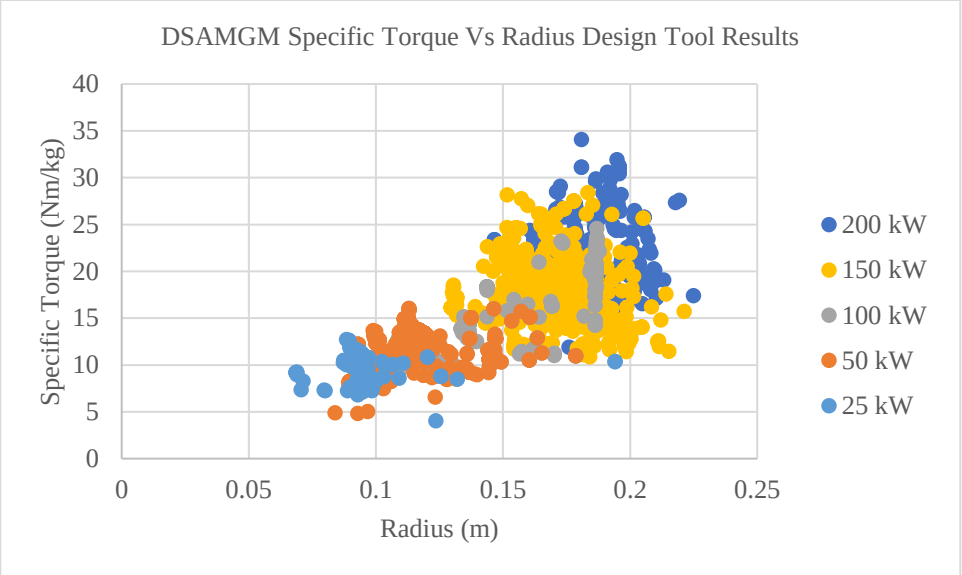

Figure 20 Specific Torque versus radius results from the revised DSAMGM design tool.

The design study results in Figure 19 show an increase in achievable specific torque and efficiency with increases in the machine's output power. This trend corresponds to the increased machine radius with increased machine power trend shown in Figure 20, where larger machines can have better aspect ratios at larger radius and correspondingly can maintain or increase performance with increased radius. Figure 21 shows the design results for specific torque versus rotational speed. A trend can be seen where lower rotational speed enables higher specific torque. This trend is primarily caused by the higher torque required at lower speed allowing for a larger radius machine. This trend may be exaggerated however as the tool was set to optimize specific torque with no limits or constraints put on rotational speed.

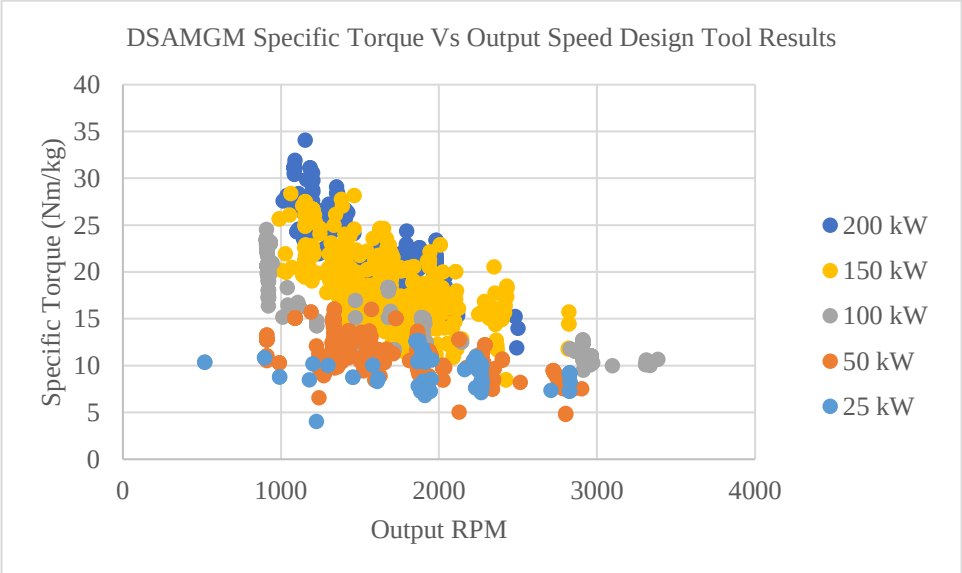

Figure 21 Results from the revised DSAMGM design tool for specific torque versus output speed.

The design tool results show the DSAMGM to be able to achieve reasonable specific torques and very high efficiencies. Compared to state-of-the-art electric aircraft motors like the Siemens SP260D and MagniX 250, which achieve around 20 Nm/kg at 93% to 95% efficiency, the DSAGMG is predicted to offer significant performance improvements. It should be noted that both of those commercial machines are higher power and larger radius machines than the DSAMGM designs considered in this paper.

Figure 22 shows a comparison of all the 100 kW outer stator magnetically-geared motor (OSMGM) results from [7] to the 100 kW results from the revised DSAMGM design tool, along with the Siemens and MagniX machines. The OSMGM is shown to be able to achieve higher specific torque than the DSAMGM at a given machine radius. This higher achievable specific torque of the OSMGM relative to the DSAMGM is believed to result from the OSMGM not compromising its magnetic gear geometry to integrate the stator while the DSAMGM must compromise its sun gear to interact with both the gear and the stator (i.e., the DSAMGM uses a north-south magnet array without back iron instead of a Halbach array).

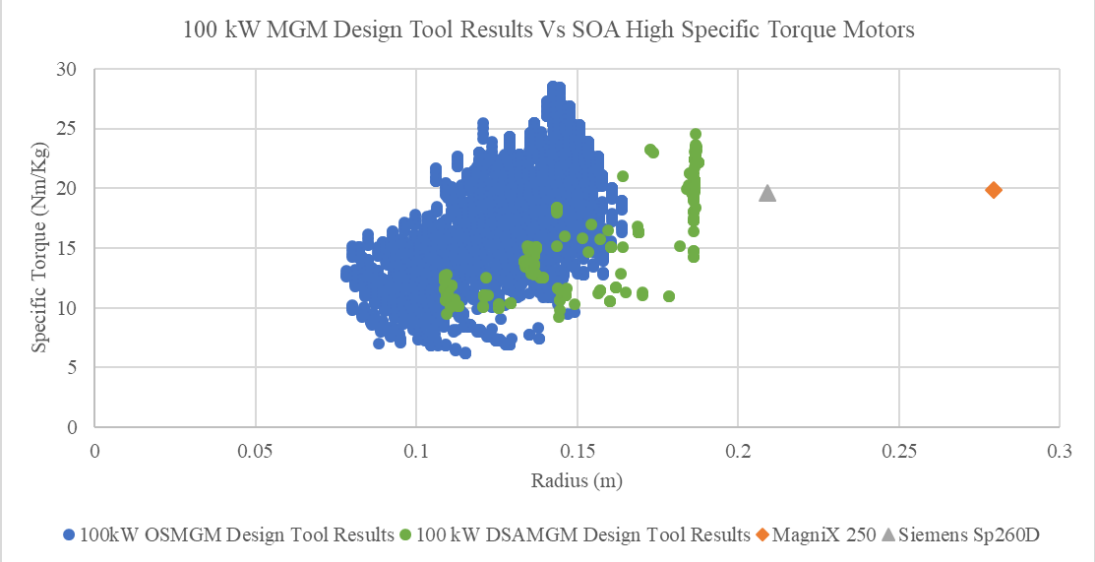

Figure 22 Comparison of 100 kW DSAMGM designs from the revised design tool to state-of-the-art commercial machines and 100 kW designs of an outer stator magnetically-geared motor from [7].

VI. Conclusion

In this paper, an assessment of double-sided axial-flux magnetically-geared motors (DSAMGM) was completed to quantify the topology's potential to achieve high specific torque and efficiency in electric aircraft applications. The DSAMGM concept was introduced and a design tool for DSAMGM was developed. High fidelity analysis of an example DSAMGM design was completed to adjust the design code's assumptions and provide more confidence in the feasibility of the DSAMGM for electric aircraft applications. The revised design tool was harnessed to quantify the achievable performance of the DSAMGM in the range of 25-200 kW. It was shown that the DSAMGM can achieve high specific torque (>20 Nm/kg) and high efficiency (>97%), suggesting that it can outperform most state-of-the-art direct drive electric motors. In comparison to the outer stator magnetically-geared motor (OSMGM), the results at 100 kW suggest the OSMGM to be the better magnetically-geared motor topology. Future work in this area targets assessment of more magnetically-geared motor topologies for electric aircraft applications, before selecting a topology for further study, prototyping, and technology advancement.

Appendix

A. Static Electromagnetic FEA Loss Calculations

To estimate the magnetic loss in the modulator, ring gear iron, and stator iron of the DSAMGM, the peak flux density in all three are exported from each FEA simulation as discussed in Section III-C. Magnetic iron loss is then calculated using the Steinmetz equation.

$$P_v = k f^{\alpha} B^{\beta}$$

Where P_v is the iron loss per volume, f is the frequency of the magnetic field, B is the peak magnetic flux density, and k, α, and β are the Stienmetz coefficients.

For the modulator, B is set to the peak flux density in the modulator in the FEA simulation and f is set to the relative passage frequency of the sun and ring gear poles on the modulator pole pieces

$$f_{sun-mod} = \frac{RPM_{sun}}{60} * \frac{GR-1}{GR} * PS = \frac{RPM_{mod}}{60} * PR = f_{ring-mod}$$

For the stator iron, the loss is broken down into back iron and tooth losses f is taken to be the frequency of the slots relative to the sun gear,

$$f_{tooth} = \frac{RPM_{sun}}{60} * Slots$$

where *slots* is the number of stator teeth. This adjusts for the rate of magnetization of each tooth as the sun gear flux passes from one tooth to the next. The loss then has to be adjusted to account for the fact that while the tooth magnetizes at a rate corresponding to this frequency, the period of repetition for its magnetization is the same as that of the back iron. So that the tooth loss definition is

$$P_{v-tooth} = \frac{f_{elec}}{f_{tooth}} k f_{tooth}^{\alpha} B^{\beta}$$

For the ring gear iron loss, f is simply taken to be the electrical frequency of the sun gear and B the peak flux density in the iron.

Ring gear magnet losses the field in the ring gear iron is used to estimate the sun gear field that reaches the ring gear. Ring gear magnet eddy current losses are then estimated using

$$P_c = \frac{1}{16}\frac{V}{\rho}\frac{w^2 l^2}{w^2 + l^2} B^2 f^2$$

where P_c is the power loss in the magnets due to eddy currents, V is the volume of a single magnet, ρ is the resistivity of the magnet material, w is the width of the magnet, and l is the length of the axial magnet laminations

Sun magnet losses are neglected in the design tool due to the difficulty in estimating them using a single, static 2D FEA. Past work by the authors has shown that magnet laminations can be used to suppress them to low values [6]. However, this is still a known source of error in the design tool's loss prediction.

B. Fluid Flow Calculations for Cooling Jacket Design

The equations for both laminar and turbulent heat transfer and fluid flow from [23] are used. Pumping losses are defined by

$$Loss_{flow} = \varphi \frac{\rho u^2}{2D} L$$

Where φ is the Moody friction factor, u is the average fluid flow velocity, ρ is the fluid density, D is the hydraulic diameter of the fluid channel, and L is the length of the fluid channel. Moody friction factor in the laminar flow regime is defined as

$$\varphi = \frac{64}{Re}$$

In the turbulent flow regime it is define as

$$\varphi = (0.790 \ln(Re) - 1.64)^{-2}$$

In both cases Re is Reynolds Number.

Nusselt number correlations are used to define the convection coefficient on the walls of the heat sink. In the laminar case Nusselt number is defined as

$$Nu_D = 1.051 \ln\left(\frac{h_{channel}}{w_{channel}}\right) + 2.89$$

In the turbulent case it is defined as

$$Nu_D = \frac{\left(\frac{\varphi}{8}\right)(Re - 1000)Pr}{1 + 12.7\left(\frac{\varphi}{8}\right)^{0.5}(Pr^{\frac{2}{3}} - 1)}$$

Where Pr is Prandtl number.

C. Pseudo Time Stepping FEA Magnetic Loss Equations

For the pseudo time stepping FEA efficiency analysis, magnet eddy currents are evaluated via the equation found in [24].

$$P_c = \frac{1}{16}\frac{V}{\rho}\frac{w^2 l^2}{w^2 + l^2}\frac{1}{T}\int_0^T \left(\frac{dB}{dt}\right)^2 dt$$

Where P_c is the power loss in the magnets due to eddy currents, V is the volume of a single magnet, ρ is the resistivity of the magnet material, w is the width of the magnet, l is the length of the axial magnet laminations, T is the period of repetition for the magnetic field, B is the magnetic flux density, and t is time.

Iron loss in both the modulator and the stator are evaluated with the improved generalized Stienmetz equation

$$P_v = \frac{M}{T}\int_0^T k_1 \left|\frac{dB}{dt}\right|^{\alpha} (\Delta B)^{\beta-\alpha} dt$$

Where P_v is the power loss in the iron, M is the mass of iron, ΔB is the peak-to-peak flux density, and $k_1, \alpha,$ and β are coefficients based on material testing data from the material's manufacturer. This equation is used instead of different iron loss evaluation methods because it has the ability to deal with minor flux loop in the iron magnetization. Minor flux loops are common in magnetic gear modulators as both the ring and sun magnets act on it.

Acknowledgments

The authors would like to acknowledge the NASA Revolutionary Vertical Lift Technology Project for sponsoring this work.

VII.References

[1] E. V. Zaretsky, *Bearing and Gear Steels for Aerospace Applications*, NASA TM 102529, NASA, 1990.

[2] D. Astridge and M. Savage, "Rotorcraft Drivetrain Life Safety and Reliability," *AGARD*, vol. 775, 1990.

[3] J. Scheidler, V. Asnani and T. Tallerico, "NASA's Magnetic Gearing Research for Electrified Aircraft propulsion," in *AIAA/IEEE Electric Aircraft Technologies Symposium*, Cincinnati, 2018.

[4] J. J. Scheidler, Z. A. Cameron and T. F. Tallerico, "Dynamic Testing of a High Specific Torque Concentric Magnetic Gear," in *Vertical Flight Society's 75th Annual Forum*, Philadelphia, 2019.

[5] T. F. Tallerico, Z. A. Cameron and J. J. Scheidler, "Design of a Magnetic Gear for NASA's Vertical Lift Quadrotor Concept Vehicle," in *AIAA/IEE Electric Aircraft Technologies Symposium*, Indianapolis, 2019.

[6] T. F. Tallerico, J. J. Scheidler and Z. A. Cameron, "Electromagnetic Mass and Efficiency of Magnetic Gears for Electrified Aircraft," in *AIAA/IEEE Electrified Aircraft Technologies Symposium*, Indinapolis, 2019.

[7] T. F. Tallerico, Z. A. Cameron, J. J. Sheidler and H. Hasseeb, "Outer Stator Magnetically-Geared Motors for Electrified Urban Air Mobility Vehicles," in *AIAA/IEEE Electric Aircraft Technologies Symposium (EATS)*, Virtual, 2020.

[8] K. Atallah, J. Rens, S. Mezani and D. Howe, "A Novel "Psuedo" Direct-Drive Brushless Permanenet Magnet Machine," *IEEE Transactions on Magnetics*, vol. 44, no. 11, 2008.

[9] Y. Fan, H. Jiang, M. Cheng and Y. Wnag, "An Improved Magnetic-Geared Permanent Magnet In-Wheel Motor for Electric Vehicles," in *IEEE Vehicle Power and Propulsion Conference*, Lille, 2010.

[10] L. L. Wange, J. X. Shen, Y. Wang and K. Wang, "A Novel Magnetic-Geared Outer-Rotor Permanent-Magnet Brushless Motor," in *4th IET Conferance on Power Electronics, Machines, and Drives*, York, 2008.

[11] S. Jia, K. Yan, D. Liang, J. Liu and J. He, "A Novel DC-Biased Current Dual PM Vernier Machine," in *IEEE International Electric Machines and Drives Conferance*, Sna Diego, 2019.

[12] A. Penzkofer and K. Atallah, "Analytical Modeling and Optimization of Pseudo-Direct Drive Permanent Magnet Machines for Large Wind Trubines," *IEEE Transactions on Magnetics*, vol. 15, no. 12, 2015.

[13] M. C. Gardner, B. E. Jack, M. Johnson and H. A. Toliyat, "Comparison of Surface Mounted Permanent Magnet Coaxial Radial Flux Magnetic Gears Independently Optimized for Volume, Cost, and Mass," *IEEE Transactions on Industry Applications*, vol. 54, no. 3, pp. 2237-2245, 2018.

[14] K. Attallah and D. Howe, "A novel high-performance magnetic gear," *IEEE Transactions on Magnetics*, vol. 37, no. 4, pp. 2844-2846, 2001.

[15] T. Lubin, S. Mezani and A. Rezzoug, "Analytical Computation of the Magnetic Field Distribution in a Magnetic Gear," *IEEE TRANSACTIONS ON MAGNETICS*, vol. 46, no. 7, 2010.

[16] K. Atallah, S. Calverley and D. Howe, "Design, Analysis, and Realization of a High-Performance Magnetic Gear," *IEEE Electirc Power Applications,* pp. 135-143, 2004.

[17] A. M. El-Refaie, "Fractional-Slot Concentrated-Windings Synochronous Permanent Magnet Machines: Opportunities and Challenges," *IEEE TRANSACTIONS ON INDUSTRIAL ELECTRONICS,* vol. 57, no. 1, 2010.

[18] M. Gardner, B. Praslicka, M. Johnson and H. A. Toliyat, "Optimization of Coaxial Magnetic Gear Design and Magnet Material Grade at Different Temperatures and Gear Ratios," *IEEE Transactions on Energy Conversion,* 2021.

[19] SKF Group, "SKF Super Precision Bearing Catalog," March 2016. [Online]. Available: https://www.skf.com/binaries/pub12/Images/0901d19680495562-Super-precision-bearings-catalogue---13383_2-EN_tcm_12-129877.pdf. [Accessed July 2020].

[20] SKF Group, "The SKF Model for Calculating the Firctional Mament," [Online]. Available: https://www.skf.com/binaries/pub12/Images/0901d1968065e9e7-The-SKF-model-for-calculating-the-frictional-movement_tcm_12-299767.pdf. [Accessed July 2020].

[21] G. Jungmayr, J. Loeffler, B. Winter, F. Jeske and W. Amrhein, "Magnetic gear: Radial Force, Cogging Torque, Skewing, and Optimization," *IEEE Transactions on Industrial Applications,* pp. 3822-3830, 2016.

[22] D. A. Howey, P. R. N. Childes and A. S. Holmes, "Air-Gap Convection in Rotating Electrical Machines," *IEEE Transactions on Industrial Electronics,* vol. 59, no. 3, 2012.

[23] T. L. Bergman, A. S. Lavine, F. P. Incropera and D. P. Dewitt, Introduction to Heat Transfer, Hoboken: John Wiley & Sons, 2011.

[24] S. Rouho, T. Santa-Norkki, J. Kolehmainen and A. Arkkio, "Modeling Magnet Length in 2-D Finite Element Analysis of Electric Machnines," *IEE Transactions on Magnetics,* vol. 45, no. 8, 2009.

[25] V. Venkatachalam, C. Sullivan, T. Abdallah and H. Tacca, "Accurate Predicition of Ferritie Core Loss with Non-Sinusoidal Waveforms Using only Steinmets Parameters," in *Computers in Power Electronics* , Mayaguez, 2002.

[26] S. Gerber and R. J. Wang, "Analysis of the End-Effects in Magnetic Gears and Magnetically Geared Machines," in *Inernational Conferance on Electical Machines Proceedings*, Berlin, 2014.

[27] K. Atallah, W. Wang, S. D. Calverley and S. Duggan, "Design and Operation of a Magnetic Continuously Variable Transmission," *IEEE Transactions on Industry Applications,* vol. 48, no. 4, 2012.